Guidance, Navigation, and Control of a Low-Altitude Nanosatellite equipped with Air-breathing Electric Propulsion

EUGENIO FERRATO
Institute of Mechanical Intelligence, Scuola Superiore Sant'Anna, Pisa, Italy

VITTORIO GIANNETTI
Institute of Mechanical Intelligence, Scuola Superiore Sant'Anna, Pisa, Italy

TOMMASO ANDREUSSI
Institute of Mechanical Intelligence, Scuola Superiore Sant'Anna, Pisa, Italy

***Abstract*—In recent years, near-Earth space utilization has seen the emergence of air-breathing electric propulsion as an enabling technology for long-duration missions conducted at very low altitudes. This work investigates the guidance, navigation, and control of a 6U CubeSat platform orbiting at altitudes below 300 km and equipped with an electrostatic air-breathing thruster. The analysis is conducted in MATLAB-Simulink and is based upon the coupling of its built-in orbital propagator with the NRLMSISE-00 atmospheric model, the recently developed ADBSat suite for computing the aerodynamic forces and torques acting on the platform, and a simplified performance model relating the propulsive performance to the inlet atmospheric properties, spacecraft attitude, and thruster operating parameters. A thrust control law, based on the feedback from the orbital elements estimated on-board and regulating the voltage applied to the screen electrode of a reference gridded air-breathing thruster, is implemented and verified.**

***Index Terms*— Air-breathing Electric Propulsion, Attitude and Orbit Control, CubeSat, Very Low Earth Orbit.**

Manuscript received XXXXX 00, 0000; revised XXXXX 00, 0000; accepted XXXXX 00, 0000. This work was supported by the the HORIZON ERC-2022-COG GA 101088694 project "Building a space Revolution: Electric Air-breathing Technology for High atmosphere Exploration (BREATHE)", CUP J53C23001840006. Views and opinions here expressed are those of the authors only and do not necessarily reflect those of the European Union nor the European Research Council. *Corresponding author: E. Ferrato*.

E. Ferrato is with the Institute of Mechanical Intelligence at Scuola Superiore Sant'Anna, Pisa, 56010, Italy (e-mail: eugenio.ferrato@santannapisa.it). V. Giannetti is with the Institute of Mechanical Intelligence at Scuola Superiore Sant'Anna, Pisa, 56010, Italy (e-mail: vittorio.giannetti@santannapisa.it). T. Andreussi is with the Institute of Mechanical Intelligence at Scuola Superiore Sant'Anna, Pisa, 56010, Italy (e-mail: tommaso.andreussi@santannapisa.it).

0018-9251 © XXXX IEEE

I. INTRODUCTION

OVER the past decade, the prospect of conducting space mission below 350 km of mean altitude (in Very Low Earth Orbits - VLEO) gained strong interest from the space community, as several studies have consistently shown how reducing the orbit altitude could be advantageous for a wide range of mission applications, including optical, radar, lidar, and telecommunication missions [1], [2], [3], [4]. Despite the complex technological challenges in terms of atmospheric drag, material compatibility with atomic oxygen, and reduced communication windows, the potential benefits of VLEO are substantial. These include improved reconnaissance conditions and link budget, lower latency, lower required transmit power, and lower environmental radiation levels. Perhaps, the most interesting feature of VLEO is that it represents an environment that can be used sustainably, since the atmospheric drag can remove unpropelled satellites and debris from orbit in a few days or weeks, hence simplifying the spacecraft end-of-life disposal and minimising the collision risk with the existing debris population [5].

Yet, the practical use of VLEO is hindered by the substantial amount of propellant a propulsion system would need to counteract the atmospheric drag for meaningful mission durations. To address the limitations of traditional space propulsion, air-breathing electric propulsion (ABEP) emerged as a potentially enabling technology for VLEO missions. This propulsion method integrates a rarefied flow air intake, engineered to efficiently collect the thin atmosphere in front of a spacecraft, with an electric thruster that ionizes and accelerates the collected gas molecules. To date, several ABEP concepts have been proposed and analysed. Numerical investigations on different air intakes designs were conducted by multiple research groups, while different approaches to ionize, accelerate, and neutralize the air propellant have been proposed and characterized [6], [7], [8]. Thanks to the development of VLEO flow simulators, the end-to-end testing of a few air-breathing systems have been performed [9], [10], [11]. Nonetheless, no ABEP prototype has yet demonstrated the capability to perform full drag compensation, neither on-ground nor in space.

In parallel, based on the available atmospheric models, several authors have investigated the aerodynamic behaviour of satellite platforms in VLEO and the feasibility of air-breathing electric propulsion systems. These studies have primarily focused on platform masses between 100 kg and 1000 kg, available power levels in the 0.3 kW to 3 kW range, and mission durations of several years on sun-synchronous orbits at altitudes below 250 km [12], [13], [14], [15], [16]. From these studies, it became evident how ABEP propulsion relies on a delicate balance with platform and mission design. Several factors must be considered in the design trade-offs, including, among others, the highly variable flow density and composition, the area available to collect the atmospheric flow, the solar array surface and orientation, the need to keep the intake aligned with the incoming flow, the constraints of payload accommodation and operation, the requirement imposed by the platform power generation capabilities, and the thruster firing strategy [17], [18].

In general, the difficulties in recreating on-ground the VLEO environment hindered the technological development of the ABEP concept. This highlighted the need for the in-orbit experimentation of the technology. On the other hand, the unpredictability and high variability of the VLEO atmosphere pose significant challenges in devising realistic, low-risk mission applications. As such, considering the significantly lower time and resources needed to design, launch and operate a nanosatellite compared to larger, non standardized platforms, prioritizing the development of air-breathing nanosatellites appears as a practical and affordable strategy to pursue the in-orbit experimentation of ABEP propulsion. Moreover, given the greater complexity in allocating propellant for drag compensation on CubeSats compared to larger platforms where more volume is available for on-board propellant storage, VLEO nanosatellites would particularly benefit from a functional air-breathing technology [18].

Based on the above considerations, in this work, we present a preliminary mission analysis aimed at verifying the capability of a 6U nanosatellite equipped with an electrostatic air-breathing thruster to maintain a given VLEO orbit for extended periods. A novel control algorithm, regulating the voltage applied to the air-breathing thruster accelerating electrode and aimed at the autonomous station-keeping of a target orbit, is proposed and verified. The analysis is conducted within the BREATHE Virtual laboratory, a numerical environment for air-breathing systems design, on-ground verification, and in-orbit operation being developed in the framework of the ERC project BREATHE [19].

Compared to previous studies in the field, the present work addresses for the first time in a fully integrated way the mission analysis of air-breathing platforms in VLEO. In general, the intensity and variability of perturbations induced by the residual atmosphere in VLEO strongly couples system design and mission analysis, making the development of analysis tools a challenging task. This is even more critical for platform based on air-breathing electric propulsion, due to the impact of space environment on thrust generation and consequently on power management. To the authors knowledge, in this research three main innovations have been introduced. First, a closed-loop integration of complex models has been achieved, including atmospheric dynamics, aerodynamic forces, and attitude sensors, allowing for a comprehensive assessment of low-altitude, air-breathing spacecraft feasibility and practical implementation. Second, a detailed study has been performed on an air-breathing CubeSat, exploiting real-world data from commercial spacecraft to explore subsystem interactions and advancing the methodology. Lastly, we introduce a novel, autonomous orbit and attitude control approach that uses real-time feedback to regulate an electrostatic ABEP system, enabling fully autonomous operation for long-duration, low-altitude missions where maintaining orbital stability, minimizing drag, and eliminating operational delays are essential for mission success. In particular, while previous studies have explored the technological challenges of ABEP deployment in VLEO [6], [7], [8], [18], [20], and proposed various mission scenarios [2], [15], [13], [16], [21], [22], [23], they lack a practical implementation of autonomous closed-loop guidance, navigation, and control (GNC) strategies. Other works exploring alternative control approaches [17], [24], [25], [26], [27] differ substantially from our method, as they typically neglect realistic atmospheric and aerodynamic modelling, do not incorporate on-board sensor feedback or filtering, and fall short of demonstrating coordinated orbit and attitude control using commercial hardware. In contrast, our work seeks to integrate the key GNC aspects related to VLEO ABEP-based missions into a unified framework, establishing a foundation for long-duration, autonomous air-breathing satellite operations in this challenging orbital regime. This work relies on available data sheets of commercial off-the-shelf components for the main platform sensor and actuators, which constitute the reference platform design outlined in Sec. IIA. The methods employed to model the spacecraft dynamics and navigation are defined in Sec. IIB and IIC. The designed attitude and orbit controllers are discussed in Sec. IIE and IIF, while Sec. IIG and IIH details the approach used in modelling the platform power subsystem and in implementing the full spacecraft model. The stability of the attitude controller is evaluated in Sec. IIIA, followed by the verification of the implemented thruster controller in Sec. IIIB via long duration orbital propagations. Based upon these results, Sec. IIIC elaborates on the requirements applicable to nanosatellite scale air-breathing propulsion systems.

II. METHODS

A. Reference Platform Design

Owing to its substantial flight heritage, we have chosen Terran Orbital's Triumph 6U nanosatellite [28] as a reference platform, envisioning it to embark a miniaturized air-breathing electric propulsion subsystem. As schematized in Fig. 1, we define the spacecraft body frame such that the roll x_B axis is parallel to the S/C longitudinal direction and directed toward the intake inlet area, the S/C yaw z_B axis is directed toward the zenith pointing S/C solar wing and the pitch y_B axis forms a right-handed orthonormal frame. The body-frame origin coincides with the geometric centre of the platform body, which is equipped with two 262 mm x 600 mm solar arrays capable of providing up to 50 W of power each in fully-illuminated condition. A mass of 14 kg and a uniform mass density distribution is considered for the simplified platform model. The nominal mission concept of operations (ConOps) foresees activity in circular dawn-

This article has been accepted for publication in IEEE Transactions on Aerospace and Electronic Systems. This is the author's version which has not been fully edited and content may change prior to final publication. Citation information: DOI 10.1109/TAES.2025.3577159

TABLE I
Technical specifications of the COTS platform components selected for this study.

Item	Parameter	Symbol	Value	Unit
Full platform	mass	$M_{S/C}$	14	kg
Terran Orbital Triumph	CoG position	$\mathbf{\Delta r_{CoG}}$	[0,0,0]	m
	$x_B x_B$ inertia	$I_{S/C,xx}$	0.466	kgm^2
	$y_B y_B$ inertia	$I_{S/C,yy}$	0.432	kgm^2
	$z_B z_B$ inertia	$I_{S/C,zz}$	0.139	kgm^2
	max. solar array power	P_{max}	100	W
4 reaction wheels	wheel inertia	I_{RW}	3e-5	kgm^2
NanoTorque GSW-600	max. torque per wheel	$\tau_{RW,sat}$	1.5e-3	Nm
in pyramidal config.	max. wheel velocity	$\omega_{RW,sat}$	6000	rpm
3-axes magnetorquers GST-600	dipole saturation per axis	$m_{MT,sat}$	0.3	Am^2
2 sun sensors NanoSense FSS	3σ accuracy	σ_{SS}	2	deg
2 star trackers arcsec Twinkle	3σ accuracy	σ_{ST}	0.03	deg
3-axes magnetometer NanoSense M315	3σ accuracy	σ_{MM}	5e-9	T
3-axes MEMS gyro	3σ noise	$\sigma_{\omega,GY}$	0.15	deg/s
InvenSense MPU-3300	3σ bias drift noise	$\sigma_{b,GY}$	0.015	deg/s^2
	bias drift time constant	$\tau_{b,GY}$	600	s
GPS NovAtel OEM-719	3σ accuracy	σ_{GPS}	4.5	m

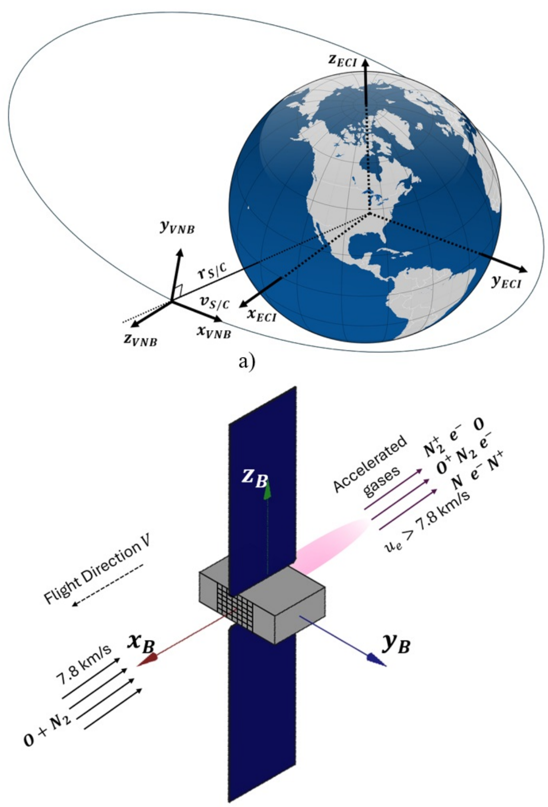

Fig. 1. a) Illustration of the spacecraft-centered Velocity-Normal-Binormal (VNB) frame. b) Simplified platform CAD model with nominal solar array orientation and body-frame definition.

dusk Sun-synchronous orbits (SSO), with a fixed solar array orientation with respect to the body-frame, and in a nominal attitude configuration such that the x_B axis is aligned with the orbital velocity direction and the z_B axis points away from Earth's ground. In a dawn-dusk SSO, such a configuration maximizes the power available with nominal solar array orientation since the sun position relative to the spacecraft would approximately be constantly aligned with the y_B body axis. The air-breathing propulsion subsystem is assumed to have an intake inlet area A_{itk} of 0.01 m^2 and to occupy the central 2U of the platform, thus leaving 4U of volume for the spacecraft payload and the other subsystems. The platform components relevant to this investigation have all been selected among available commercial off-the-shelf (COTS) solutions. In this regard, Table I reports the specification of the chosen platform sensors and actuators.

B. Spacecraft Dynamics

The spacecraft equations of motion are described with respect to the Earth-centered inertial (ECI) frame, in which the x_{ECI}–y_{ECI} plane coincides with the equatorial plane of Earth, the x_{ECI} axis is permanently fixed in a direction relative to the celestial sphere, and the z_{ECI} axis lies at a 90° angle to the equatorial plane and extends through the North Pole. Accordingly, the equations describing the spacecraft orbital dynamics in the ECI frame are

$$\dot{\mathbf{r}}_{ECI} = \mathbf{v}_{ECI} \tag{1}$$

$$\dot{\mathbf{v}}_{ECI} = -\mu \frac{\mathbf{r}_{ECI}}{|r_{ECI}|^3} + \mathbf{a}_g + \mathbf{a}_d + \frac{\mathbf{D}_{ECI}}{M_{S/C}} + \frac{\mathbf{T}_{ECI}}{M_{S/C}}, \tag{2}$$

where $\mathbf{r}_{ECI}$ and $\mathbf{v}_{ECI}$ respectively identify the instantaneous spacecraft position and velocity in the ECI frame, μ

is Earth's gravitational parameter, $M_{S/C}$ is the spacecraft mass, $\mathbf{a}_g$ represents the impact of Earth's gravity field harmonics, modeled here as spherical harmonics up to the 120th degree according to the EGM2008 model [29]. The term $\mathbf{a}_d$ represents minor perturbations, such as lunisolar attraction and solar radiation pressure. These minor perturbations are neglected here because they are several orders of magnitude lower than the accelerations induced by the propulsion thrust $\mathbf{T}$ and the atmospheric drag $\mathbf{D}$ characterizing VLEO altitudes [30].

The spacecraft attitude dynamics is described by

$$\dot{\mathbf{q}}_{ECI2B} = \frac{1}{2}\begin{bmatrix} 0 \\ \boldsymbol{\omega}_{ECI2B} \end{bmatrix} \circ \mathbf{q}_{ECI2B} \tag{3}$$

$$\dot{\boldsymbol{\omega}}_{ECI2B} = \mathbf{I}_{S/C}^{-1}(\boldsymbol{\tau}_g + \boldsymbol{\tau}_e + \boldsymbol{\tau}_D + \boldsymbol{\tau}_T + \boldsymbol{\tau}_a - \boldsymbol{\omega}_{ECI2B} \times \mathbf{I}_{S/C}\boldsymbol{\omega}_{ECI2B}), \tag{4}$$

where $\circ$ is the quaternion multiplication operator and the attitude quaternion $\mathbf{q}_{ECI2B}$ represents the spacecraft body axes orientation with respect to the inertial ECI frame. $\boldsymbol{\omega}_{ECI2B}$ is the spacecraft angular velocity relative to the ECI frame expressed in the body-frame, $\mathbf{I_{S/C}}$ is the spacecraft inertia matrix, $\boldsymbol{\tau}_g$ is the gravity-gradient torque, $\boldsymbol{\tau}_e$ is the torque (here neglected) induced by the minor perturbations such as solar pressure and lunisolar gravity gradients, $\boldsymbol{\tau}_D$ is the aerodynamic disturbance torque, $\boldsymbol{\tau}_T$ is the residual torque produced during thruster firing depending on the relative CoG-thruster position, and $\boldsymbol{\tau}_a$ is the torque applied by the spacecraft attitude actuators. All torques are expressed in the spacecraft body-frame.

The reference mission ConOps continuously tasks the platform attitude controller with maintaining the body axes aligned with the Velocity-Normal-Binormal (VNB) frame, a spacecraft-centered frame illustrated in Fig. 1a and defined as

$$\mathbf{x}_{VNB} = \mathbf{v}_{ECI}/|v_{ECI}| \tag{5}$$

$$\mathbf{y}_{VNB} = \mathbf{r}_{ECI} \times \mathbf{v}_{ECI}/|\mathbf{r}_{ECI} \times \mathbf{v}_{ECI}| \tag{6}$$

$$\mathbf{z}_{VNB} = \mathbf{x}_{VNB} \times \mathbf{y}_{VNB}. \tag{7}$$

For circular orbits and consistently with the platform configuration under investigation, the VNB orientation ensures the minimization of the frontal area non-contributing to propellant collection (such as solar arrays) directly exposed to the atmospheric flow, favorable illumination condition for the solar arrays, optimal alignment between flow direction and intake axis, and good ground observation conditions for the embarked payload. Hence, the attitude controller is based upon the feedback of the $\mathbf{q}_{VNB2B}$ quaternion, representing the rotation between the VNB and body frame, and the body angular velocity $\boldsymbol{\omega}_{VNB2B}$ relative to the VNB frame. In the following, the subscripts will be omitted when referring to the VNB to body quaternion and angular velocity. The goal of the attitude control is thus to maintain the condition $\mathbf{q} = [1, 0, 0, 0]$ and $\boldsymbol{\omega} = [0, 0, 0]$.

C. Navigation

The nanosatellite is equipped with two sun sensors, two star trackers, a GPS, a digital gyro, and a set of three magnetometers measuring the local Earth's magnetic field $\mathbf{B}$ in the spacecraft body-frame. In addition, an encoder determines the reaction wheel angular momentum $\mathbf{h}_{RW}$, here defined as a four components vector representing the magnitude and direction of the angular momentum along each of the four wheels rotation axis. All these measurements are implemented in an Extended Kalman Filter (EKF) [31]. In more detail, the sun sensors and the star trackers are used to determine the attitude orientation of the spacecraft. For small error angles, each sun sensor and star tracker outputs the value

$$\check{\mathbf{y}}_{SS} = \begin{bmatrix} 1 \\ \boldsymbol{\upsilon}_{SS}/2 \end{bmatrix} \circ \mathbf{q}_{ECI2B} \tag{8}$$

$$\check{\mathbf{y}}_{ST} = \begin{bmatrix} 1 \\ \boldsymbol{\upsilon}_{ST}/2 \end{bmatrix} \circ \mathbf{q}_{ECI2B} \tag{9}$$

where the notation $\check{}$ indicates a measurement reading and $\boldsymbol{\upsilon}$ is the measurement noise, here set as a Gaussian white noise with power σ_{SS}^2 and σ_{ST}^2, σ^2 being the mean square deviation defining the measurement accuracy. In the assumption of statistically independent readings, we express the associated measurement covariance as a diagonal matrix:

$$\boldsymbol{\Upsilon}_{SS} = \sigma_{SS}^2 \mathbf{I}_{3x3} \tag{10}$$

$$\boldsymbol{\Upsilon}_{ST} = \sigma_{ST}^2 \mathbf{I}_{3x3}, \tag{11}$$

where $\mathbf{I}_{3x3}$ is the 3x3 identity matrix. Since the measurement covariance of the star trackers is significantly smaller than that of the sun sensors, the EKF primarily relies on star tracker data, with the sun sensors influencing the estimated spacecraft state only in the case of star tracker failure. In parallel, the GPS, magnetometer, and reaction wheels encoder output the readings

$$\check{\mathbf{y}}_{GPS} = \mathbf{r}_{ECI} + \boldsymbol{\upsilon}_{GPS} \tag{12}$$

$$\check{\mathbf{y}}_{MM} = \mathbf{B} + \boldsymbol{\upsilon}_{MM} \tag{13}$$

$$\check{\mathbf{y}}_{RW} = \mathbf{h}_{RW} + \boldsymbol{\upsilon}_{RW}, \tag{14}$$

with associated Gaussian white noise $\boldsymbol{\upsilon}$ and diagonal covariance matrices $\boldsymbol{\Upsilon}$ with noise power defined consistently with the mean square deviation of the sensor measurement accuracy. Moreover, as gyro measurements are typically affected by a drifting bias noise, the gyro reading is expressed as

$$\check{\mathbf{y}}_{GY} = \boldsymbol{\omega}_{ECI2B} + \mathbf{b}_{\omega} + \boldsymbol{\upsilon}_{\omega,GY}, \tag{15}$$

where the gyro bias $\mathbf{b}_{\omega}$ is described by a Ornstein–Uhlenbeck process [32] with time constant $\tau_{b,GY}$:

$$\dot{\mathbf{b}}_{\omega} = -\frac{\mathbf{b}_{\omega,GY}}{\tau_{b,GY}} + \boldsymbol{\upsilon}_{b,GY}, \tag{16}$$

with associated noise covariance matrices

$$\boldsymbol{\Upsilon}_{\omega,GY} = \sigma_{\omega,GY}^2 \mathbf{I}_{3x3} \tag{17}$$

$$\boldsymbol{\Upsilon}_{b,GY} = \sigma_{b,GY}^2 \mathbf{I}_{3x3}. \tag{18}$$

A reduced spacecraft state $\mathbf{s}$, defined as the 16-elements vector

$$\mathbf{s} = [\mathbf{r}_{ECI}, \mathbf{v}_{ECI}, \mathbf{q}_{ECI2B}, \boldsymbol{\omega}_{ECI2B}, \mathbf{b}_{\omega}], \tag{19}$$

is implemented in the EKF, which every Δt seconds updates the estimated spacecraft state variables, denoted with the notation $\hat{}$, as

$$\hat{\mathbf{s}} = [\hat{\mathbf{r}}_{ECI}, \hat{\mathbf{v}}_{ECI}, \hat{\mathbf{q}}_{ECI2B}, \hat{\boldsymbol{\omega}}_{ECI2B}, \hat{\mathbf{b}}_{\omega}] \tag{20}$$

based on the prediction and sensor models

$$\hat{\mathbf{s}}_k^- = f(\hat{\mathbf{s}}_{k-1}, \mathbf{w}_{k-1}) \tag{21}$$

$$\check{\mathbf{y}}_k = g(\mathbf{s}_k, \boldsymbol{\upsilon}_k), \tag{22}$$

where the notation $\hat{\mathbf{s}}_k^-$ represents the prediction state variable estimate at time-step k, $\check{\mathbf{y}}_k$ is the measurement output at time-step k, and $\mathbf{w}$ and $\boldsymbol{\upsilon}$ are the process and measurement noise, respectively.

The implemented EKF is based upon the following prediction model:

$$\hat{\mathbf{r}}_{ECI,k}^- = \hat{\mathbf{r}}_{ECI,k-1} + \hat{\mathbf{v}}_{ECI,k-1}\Delta t \tag{23}$$

$$\hat{\mathbf{v}}_{ECI,k}^- = \hat{\mathbf{v}}_{ECI,k-1} + \left(-\mu\frac{\hat{\mathbf{r}}_{ECI,k-1}}{|\hat{r}_{ECI,k-1}|^3} + \mathbf{a}_{J2}(\hat{\mathbf{r}}_{ECI,k-1})\right)\Delta t, \tag{24}$$

$$\hat{\mathbf{q}}_{ECI2B,k}^- = \hat{\mathbf{q}}_{ECI2B,k-1} + \frac{1}{2}\begin{bmatrix} 0 \\ \hat{\boldsymbol{\omega}}_{ECI2B,k-1}\end{bmatrix} \circ \hat{\mathbf{q}}_{ECI2B,k-1}\Delta t \tag{25}$$

$$\hat{\boldsymbol{\omega}}_{ECI2B,k}^- = \hat{\boldsymbol{\omega}}_{ECI2B,k-1} \tag{26}$$

$$\hat{\mathbf{b}}_{\omega,k}^- = \hat{\mathbf{b}}_{\omega,k-1} - \frac{\hat{\mathbf{b}}_{\omega,k-1}}{\tau_b}\Delta t \tag{27}$$

where $\mathbf{a}_{J2}$ is the acceleration due to the Earth's J2 gravitational harmonic. The prediction model assumes that the orbit and attitude controller are able to compensate for the external disturbances, which are thus not directly modeled in the prediction model. Specifically, in the EKF prediction model we consider the attitude actuators to be capable of maintaining the spacecraft body axes perfectly aligned with the VNB frame, whose angular velocity relative to the ECI frame is time-invariant for circular orbits as described by equation 26. Disturbances to the state vector dynamics are still accounted for by associating a process noise $\mathbf{w}$ to each state variable, from which a covariance matrix $\mathbf{W}$ is constructed.

At each time-step, the filter numerically computes the state-transition matrix $\mathbf{F}$ and the observation matrix $\mathbf{H}$

$$\mathbf{F}_{k-1} = \frac{\partial f}{\partial \mathbf{s}}\Big|_{\hat{\mathbf{s}}_{k-1}} \tag{28}$$

$$\mathbf{H}_k = \frac{\partial g}{\partial \mathbf{s}}\Big|_{\hat{\mathbf{s}}_k^-} \tag{29}$$

and updates the predicted error covariance matrix $\mathbf{P}$ and Kalman gains $\mathbf{K}$

$$\mathbf{P}_k^- = \mathbf{F}_{k-1}\mathbf{P}_{k-1}\mathbf{F}_{k-1}^T + \mathbf{W} \tag{30}$$

$$\mathbf{K}_k = \mathbf{P}_k^-\mathbf{H}_k^T(\mathbf{H}_k\mathbf{P}_k^-\mathbf{H}_k^T + \boldsymbol{\Upsilon})^{-1}, \tag{31}$$

where the measurement noise covariance matrix $\boldsymbol{\Upsilon}$ is constructed from the noise covariance of the sensors measuring the spacecraft state $\mathbf{s}$. Finally, the estimated state at time-step k is obtained by

$$\hat{\mathbf{s}}_k = \hat{\mathbf{s}}_{\mathbf{k}}^- + \mathbf{K}_k(\check{\mathbf{y}}_k - g(\hat{\mathbf{s}}_k^-, \mathbf{w}_k)), \tag{32}$$

and the predicted error covariance is propagated for the next estimate as

$$\mathbf{P}_k = (\mathbf{I} - \mathbf{K}_k\mathbf{H}_k)\mathbf{P}_{k-1}^-. \tag{33}$$

The remaining navigation variables are not directly implemented in the EKF but are instead directly related to the sensor measurement as

$$\hat{\mathbf{B}} = \check{\mathbf{B}} \tag{34}$$

$$\hat{\mathbf{h}}_{RW} = \check{\mathbf{h}}_{RW}. \tag{35}$$

At each time-step, the estimated spacecraft velocity and position are used to determine the six orbital elements, including the semi-major axis $\hat{a}$, the eccentricity $\hat{e}$, the argument of periapsis $\hat{\varphi}$, and the true anomaly $\hat{\nu}$ upon which the propulsion system control is based (see Sec. IIF). Moreover, the estimated spacecraft state is used to estimate the attitude quaternion and angular velocity with respect to the VNB frame, as follows:

$$\hat{\mathbf{q}} = \mathbf{q}_{VNB2ECI}(\hat{\mathbf{r}}_{ECI}, \hat{\mathbf{v}}_{ECI}) \circ \hat{\mathbf{q}}_{ECI2B} \tag{36}$$

$$\hat{\boldsymbol{\omega}} = \hat{\mathbf{q}}_{ECI2B}^{-1}\begin{bmatrix} 0 \\ \boldsymbol{\omega}_{VNB2ECI}(\hat{\mathbf{r}}_{ECI}, \hat{\mathbf{v}}_{ECI})\end{bmatrix}\hat{\mathbf{q}}_{ECI2B} + \hat{\boldsymbol{\omega}}_{ECI2B}, \tag{37}$$

where $\mathbf{q}_{VNB2ECI}$ and $\boldsymbol{\omega}_{VNB2ECI}$ represent the quaternion and angular velocity that transform from the VNB to the ECI reference frames. These are computed using equations (5)-(7) from the estimated spacecraft position and velocity in the ECI frame. These values are then applied to the estimated spacecraft attitude in the ECI frame to estimate the spacecraft body axis orientation $\hat{\mathbf{q}}$ and angular velocity $\hat{\boldsymbol{\omega}}$ relative to the VNB frame, which will serve as error feedback for the attitude controller.

D. Platform Aerodynamics

Aerodynamic forces and torques due to the residual atmospheric gases are the main source of disturbance in VLEO orbits. In this work, we make use of the NRLMSISE-00 [33] reference atmospheric database coupled with the recently developed ADBSat suite [34] to model the aerodynamic disturbances acting on the spacecraft. ADBSat is a software based on a novel implementation of a panel method which is capable of determining the aerodynamic properties of bodies in free-molecular flow. The full spacecraft geometry illustrated in Figure 1, inclusive of both the platform 6U body and the two high-power solar arrays, was imported in the ADBSat software. Consistently with the validation approach presented in [35], we employed the Sentman GSI model with a wall accommodation coefficient $\alpha_W = 0.9$ and a wall temperature $T_W = 300$ K, chose 19 January 2015 midnight

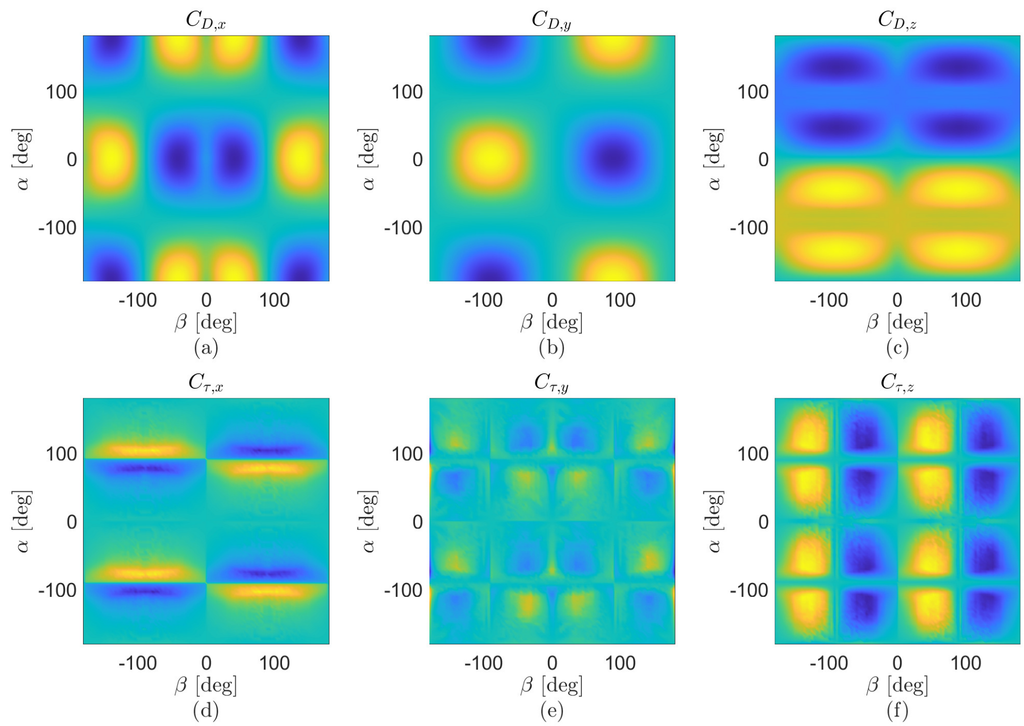

Fig. 2. Computed drag force coefficients along: a) the x-body axis, b) the y-body axis, and c) the z-body axis, and computed torque coefficients along: d) the x-body axis, e) the y-body axis, and f) the z-body axis, all shown as a function of the angle of attack α and sideslip angle β for the platform geometry under investigation. The reference spacecraft length and frontal area are set to $L_{S/C} = 0.2\ m$ and $A_f = 0.03\ m^2$.

0°/0° latitude/longitude as reference time and geographic coordinates, and set the 81-day average F10.7 to 138.1, the daily F10.7 to 121.7, and the Ap magnetic indices in the 2.9 to 9.0 range as per ADBSat default settings. Considering the aerodynamic coefficients dependence on the flow properties variations to be second-order and in any case comparable with the uncertainties related to the other model parameters (such as wall accommodation and temperature [18], [36]), the drag and torque coefficients are modeled as a function of the wind angles only, hence expressing the aerodynamic force and torque in the spacecraft body-frame as

$$\mathbf{D} = \frac{1}{2}\mathbf{C_D}(\alpha,\beta)A_f u_\infty^2 \sum_s n_{\infty,s} M_s \tag{38}$$

$$\boldsymbol{\tau}_D = \frac{1}{2}\mathbf{C}_\tau(\alpha,\beta)A_f L_{S/C} u_\infty^2 \sum_s n_{\infty,s} M_s + \boldsymbol{\Delta}\mathbf{r_{CoG}} \times \mathbf{D} \tag{39}$$

where A_f is the spacecraft frontal area, $L_{S/C}$ is the spacecraft length, $n_{\infty,s}$ is the asymptotic s-species number density, u_∞ is the magnitude of the flow velocity relative to the spacecraft, M_s is the s-species molecular mass, α is the angle of attack and β is the sideslip angle. As ADBSat assumes the center of gravity to coincide with the geometric center, the last term of (39) represents the torque due to CoG deviations. The $\mathbf{C_D}$ and $\mathbf{C}_\tau$ coefficients are three-elements vectors respectively quantifying the drag and torque components along the roll, pitch, and yaw body axes. The flow velocity relative to the spacecraft is computed in the body frame as

$$\mathbf{u}_\infty = \mathbf{q}_{ECI2B}^{-1} \circ (\mathbf{v}_{ECI} + \mathbf{u}_{HW}) \circ \mathbf{q}_{ECI2B}; \tag{40}$$

where $\mathbf{u}_{HW}$ represents the horizontal ionospheric wind velocity in the ECI frame, estimated using the HWM14 wind model [37]. Accordingly, the wind angles are calculated as follows:

$$[\alpha,\beta] = \left[\arcsin\left(\frac{u_{\infty,z}}{u_{\infty,x}}\right), \arcsin\left(\frac{u_{\infty,y}}{u_{\infty,x}}\right)\right]. \tag{41}$$

Typically, horizontal wind speeds range from 50 to 500 m/s, resulting in deviations relative to the spacecraft motion in the order of 1 to 2 deg. Fig. 2 shows the resulting aerodynamic coefficients vs wind angles as computed for the reference platform geometry described in Sec. IIA.

E. Attitude Actuators and Control

The platform is equipped with four pyramidal reaction wheels, providing a control torque $\boldsymbol{\tau}_{RW}$ for attitude maintenance and maneuvers. At the same time, a set of magnetorquers provides a torque $\boldsymbol{\tau}_{MT}$ for reaction wheel desaturation. In the spacecraft body-frame, the commanded reaction wheel torque is controlled according to a quaternion-based feedback [38]:

$$\boldsymbol{\tau_{RW}} = -k_{p,RW}\hat{q}_0\hat{\mathbf{q}} - k_{d,RW}\hat{\boldsymbol{\omega}} - \hat{\boldsymbol{\omega}}_{ECI2B} \times \mathbf{C}_{RW}\hat{\mathbf{h}}_{RW}, \tag{42}$$

where the three terms in the right-hand side respectively represents the proportional control with gain $k_{p,RW}$, the derivative control with gain $k_{d,RW}$, and a component

This article has been accepted for publication in IEEE Transactions on Aerospace and Electronic Systems. This is the author's version which has not been fully edited and content may change prior to final publication. Citation information: DOI 10.1109/TAES.2025.3577159

compensating the gyroscopic torques induced by the total reaction wheels angular momentum. The latter is expressed as the cross product of the estimated spacecraft angular velocity $\hat{\omega}_{ECI2B}$ and the instantaneous reaction wheel angular momentum in the spacecraft body frame, computed as $\mathbf{C}_{RW}\hat{\mathbf{h}}_{RW}$, where $\mathbf{C}_{RW}$ is the reaction wheel configuration matrix. For the case of four reaction wheels in a pyramidal configuration and in the assumption of negligible mounting errors, $\mathbf{C}_{RW}$ is expressed as

$$\mathbf{C}_{RW} = \begin{bmatrix} -\sqrt{3}/2 & \sqrt{3}/2 & 0 & 0 \\ 0 & 0 & -\sqrt{3}/2 & \sqrt{3}/2 \\ 0.5 & 0.5 & 0.5 & 0.5 \end{bmatrix}. \quad (43)$$

The instantaneous angular momentum of each reaction wheel is computed as

$$\dot{\mathbf{h}}_{RW} = I_{RW}\dot{\boldsymbol{\omega}}_{RW} = -\mathbf{C}^{\dagger}_{RW}\boldsymbol{\tau}_{RW}, \quad (44)$$

with the initial condition $\boldsymbol{\omega}_{RW}(0) = \boldsymbol{\omega}_{RW,0}$ and where $\mathbf{C}^{\dagger}_{RW}$ is the pseudo-inverse wheels configuration matrix, I_{RW} is the wheel inertia, and $\boldsymbol{\omega}_{RW}$ is a four component vector representing the angular velocity magnitude and direction of each wheel along its rotation axis. Wheels saturation is accounted for by imposing the non-linear constraints (i representing the i-th reaction wheel)

$$|\dot{\boldsymbol{\omega}}_{RW,i}| < \frac{\tau_{RW,sat}}{I_{RW}} \quad (45)$$

$$|\boldsymbol{\omega}_{RW,i}| < \omega_{RW,sat}, \quad (46)$$

where $\tau_{RW,sat}$ is the saturation torque and $\omega_{RW,sat}$ is the maximum rotational speed allowed by design for each wheel.

In parallel, a controller drives a set of three magnetorquers aligned with the spacecraft body axes for reaction wheels desaturation. The magnetorquers dipole moment is controlled based on the reaction wheel angular momentum $\hat{\mathbf{h}}_{RW}$ and measured Earth's magnetic field $\hat{\mathbf{B}}$ expressed in the spacecraft body-frame, as follows:

$$\mathbf{m}_{MT} = \frac{\hat{\mathbf{B}}}{|\hat{B}|^2} \times (-k_{MT}\mathbf{C}_{RW}\hat{\boldsymbol{h}}_{RW}), \quad (47)$$

where k_{MT} is the magnetorquers control gain, which results into a torque level

$$\boldsymbol{\tau}_{MT} = \mathbf{m}_{MT} \times \mathbf{B}. \quad (48)$$

Magnetorquers saturation is applied via the non-linear constraint

$$|\mathbf{m}_{MT,i}| < m_{MT,sat}, \quad (49)$$

where $m_{MT,sat}$ is the saturation dipole moment.

Accordingly, the total torque $\boldsymbol{\tau_a}$ imparted by the attitude control system to the spacecraft is

$$\boldsymbol{\tau_a} = \mathbf{m}_{MT} \times \mathbf{B} - \mathbf{C}_{RW}\dot{\mathbf{h}}_{RW} - \boldsymbol{\omega}_{ECI2B} \times \mathbf{C}_{RW}\mathbf{h}_{RW}. \quad (50)$$

F. Air-breathing Electric Propulsion and Orbit Control

Air-breathing electric propulsion makes use of the residual atmospheric particles in front of the spacecraft to produce thrust. A rarefied flow air intake collects and transmits the particles into the thruster volume, in which they are ionized and accelerated to high exhaust velocities. The intake inlet area A_{itk} occupies a fraction of the platform frontal area A_f, and the asymptotic air mass flow rate intercepting the intake inlet is

$$\dot{m}_{itk} = A_{itk}u_\infty \max(0, \cos\alpha\cos\beta)\sum_s n_{\infty,s}M_{\infty,s}, \quad (51)$$

which significantly depends on both spacecraft attitude and environmental conditions. Still, only a fraction of the mass flux is actually accepted into and accelerated by the thruster, due to the scattering behaviour of the gas particles with walls in the rarefied flow regime and to the actual thruster capability of ionizing the gathered flow before it effuses out from the thruster control volume [39], [40], [41], [42], [43]. This defines a first fundamental parameter for quantifying the performance of the air-breathing propulsion subsystem, that is the flow collection efficiency η_c and is defined as

$$\dot{m}_{thr} = \eta_c\dot{m}_{itk}. \quad (52)$$

η_c is expected to be sensitive to the flow direction relative to the spacecraft, flow properties in terms of density and composition, thruster geometry, and operating parameters, and should thus be determined by complex DSMC and plasma simulations [44], [45], [46], [47] which are beyond the scope of this work. In the result section, we present the impact on the system behaviour for constant values of η_c ranging from 0.2 to 0.4 [6]. We assume the collected and ionized mass flow to be extracted and accelerated though an electrostatic grid system at an exhaust velocity u_e of

$$u_e = \gamma\sum_s n_{thr,s}\sqrt{\frac{2e\phi}{M_s}} / \sum_s n_{thr,s} \quad (53)$$

where ϕ is the applied acceleration voltage, e is the elementary electron charge, γ is a parameter quantifying losses such as poor ion focusing and plume divergence, and $n_{thr,s}$ represents the s-species number density at grid extraction. The relation between the flow composition at intake inlet and at grid extraction will again depend on complex physical processes [23], [48]. For the purpose of this analysis, we set a constant value of the thrust loss parameter $\gamma = 0.9$ and consider the two extreme cases in which no molecular dissociation and full dissociation of the accepted atmospheric flow occurs, in the assumption of an equivalent transmission into the thruster of all the impinging atmospheric species.

Assuming the thruster to be perfectly aligned with the spacecraft geometric centre and longitudinal axis, the produced thrust in the spacecraft body-frame is computed as

$$\mathbf{T} = [\dot{m}_{thr}u_e, 0, 0], \quad (54)$$

with an associated body torque of

$$\boldsymbol{\tau_T} = \mathbf{\Delta r_{CoG}} \times \mathbf{T}. \tag{55}$$

The propulsion subsystem power consumption is estimated by introducing the thrust efficiency η_T, which quantifies the capability of the system to convert electrical power into kinetic power useful to thrust:

$$P = \frac{\dot{m}_{thr} u_e^2}{2\eta_T}, \tag{56}$$

with typical values of thrust efficiencies ranging between $\eta_T = 0.1$ and $\eta_T = 0.5$ for mature electric propulsion systems [49], [50].

In the proposed platform architecture, the thruster is continuously operated and the acceleration voltage is regulated based on the spacecraft position and velocity, thus orbital parameters, estimated by the GPS. The acceleration voltage control directly affects the instantaneous thrust and power consumption of the propulsion subsystem, and it is regulated according to the following law:

$$\phi = \phi_0 + \sqrt{\frac{\hat{a}}{\mu}} \begin{bmatrix} \hat{a} \\ \cos(\hat{\nu} + \hat{\varphi}) \cos \hat{\varphi} \\ \sin(\hat{\nu} + \hat{\varphi}) \sin \hat{\varphi} \end{bmatrix}^T \begin{bmatrix} k_a(\bar{a} - \hat{a}) \\ k_e(\bar{e} - \hat{e}) \\ k_e(\bar{e} - \hat{e}) \end{bmatrix} + k_i \int (\bar{a} - \hat{a}) dt, \tag{57}$$

where ϕ_0 is the voltage offset, k_a is the semi-major axis proportional gain, k_e is the eccentricity proportional gain, k_i is the semi-major axis integral gain, and $\bar{a}$ and $\bar{e}$ are the target semi-major axis and orbit eccentricity to be maintained, respectively. A thruster nominal acceleration voltage $\phi_0 = 1500$ V and an operating envelope in the 1000 V to 3000 V range is assumed, translating into a non-linear saturation constraint for the control equation above. The proposed control algorithm is defined consistently with previous investigations on low-Earth orbit maintenance and formation flying via low-thrust propulsion [51], [52], [53], [54], where an equivalent law is used to continuously regulate the in-track thrust level based on the orbital elements feedback. However, since both the mass flow rate processed and thrust produced by air-breathing thrusters are not likely to be measurable neither directly adjustable, in this work we adapt the same law to regulate the thruster acceleration voltage instead.

G. Electrical Power Subsystem

A complete modelization of the electrical power subsystem, inclusive of detailed solar arrays electric and battery management models, is beyond the scope of this work. Considering the very short eclipse duration, in the order of a few minutes, characterizing dawn-dusk SSO orbits, we assume the battery management system to be capable of ensuring battery survival and nominal operation of the propulsion and the other platform subsystems during eclipses. At current stage, we thus limit ourselves to estimate the power available from the solar arrays during orbit propagation and compare it to the power consumption of the air-breathing propulsion system, verifying the thruster compliance with the platform power budget. The power P_{SA} produced by the solar arrays is estimated as

$$P_{SA} = c_{ecl} P_{max} \max(0, \mathbf{n}_{SA,B} \cdot \mathbf{n}_{\odot,B}) \tag{58}$$

where $P_{max} = 100$ W is the available power in full illumination condition, $\mathbf{n}_{SA,B} = [0, -1, 0]$ is the solar array normal in the spacecraft body-frame, $\mathbf{n}_{\odot,B}$ is the relative sun position versor in the spacecraft body-frame, and c_{ecl} is a conditional multiplier set to 0 during eclipse and to 1 otherwise. The sun direction relative to the body frame is determined from the sun ephemeris $\mathbf{r}_{\odot,ECI}$, as follows:

$$\mathbf{n}_{\odot,B} = \mathbf{q}_{ECI2B}^{-1} \circ \begin{bmatrix} 0 \\ \frac{\mathbf{r}_{\odot,ECI} - \mathbf{r}_{ECI}}{|\mathbf{r}_{\odot,ECI} - \mathbf{r}_{ECI}|} \end{bmatrix} \circ \mathbf{q}_{ECI2B}. \tag{59}$$

Similarly, the c_{ecl} conditional multiplier is computed from the known spacecraft position and sun ephemeris relative to the ECI frame, using the approximation of a cylindrical shadow model and oblate ellipsoid Earth.

H. Model Implementation

We implemented the air-breathing spacecraft model in Matlab/Simulink. The first-level model architecture, shown in Fig. 3, is structured upon a spacecraft dynamics and orbit environment submodel connected to the other submodels accounting for navigation, guidance, control, actuators performance and aerodynamic disturbances.

The orbit environment submodel is based upon the built-in Matlab spacecraft dynamics block, which solves for the spacecraft orbit and attitude motion as detailed in Sec. IIB. Given the initial orbital elements and attitude orientation, platform mass properties, and time-varying body forces and torques, the spacecraft dynamic block outputs the spacecraft state in terms of spacecraft position $\mathbf{r}_{ECI}$, velocity $\mathbf{v}_{ECI}$, attitude quaternion $\mathbf{q}_{ECI2B}$, angular velocity $\boldsymbol{\omega}_{ECI2B}$, and UTC simulation time. These variables serve as input for the implemented NRMLSISE-00 atmospheric model [33], the HWM14 horizontal wind model [37], the IGRF-13 magnetic field model [55], and the DE421 Sun ephemeris dataset [56].

The spacecraft state and Earth's magnetic field are provided to the navigation submodel, which implements the Matlab built-in EKF programmed as described in Sec. IIC. The navigation state and guidance set-point are then transmitted to the control subsystem, which computes the commanded ABEP voltage, reaction wheels torques and magnetorquers dipoles.

From the received control commands, spacecraft state, and environmental properties, the actuators submodel computes the angular momentum of each reaction wheel, the actuators body torques, and the ABEP thrust and power consumption as outlined in Sec. IIE and IIF. In parallel, the disturbance submodel makes use of the input spacecraft state and atmosphere properties to evaluate the drag and torque acting on the platform. The two are computed according to (38) and (39), where the six

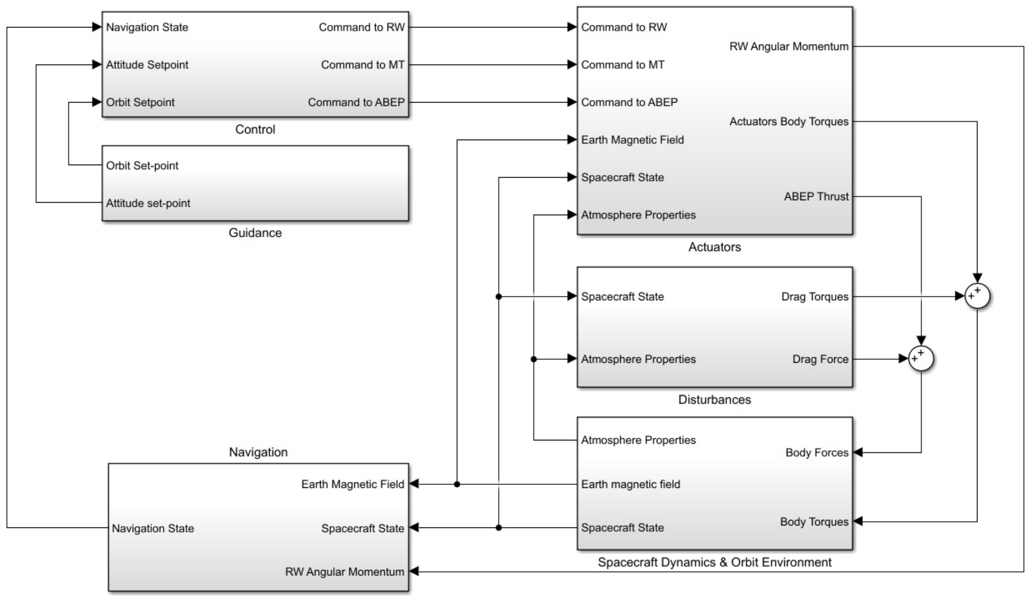

Fig. 3. Model implementation in Simulink.

force and torque coefficients are evaluated from a look-up table constructed based on the ADBSat simulation data depicted in Fig. 2.

Finally, the loop is closed by summing up the resulting actuators and aerodynamic forces and torques, providing them as input to the spacecraft dynamics & orbit environment submodel.

III. RESULTS

A. Attitude Control and Stability

We simulated the spacecraft attitude behaviour for an EKF sample time of $\Delta t = 1$ s. In this regard, all sensors used (see Table I) are compatible with a 1 Hz update rate according to their datasheets [57], [58], [59], [60], [61], [62], [63]. The attitude control gains were manually tuned until control stability was reached for a vast range of initial and environmental conditions, resulting in the setting $k_{p,RW}$ = 3e-3 Nm, $k_{d,RW}$ = 1.8e-3 Nms, and k_{MT} = 8.7e-4 s. As an example, Fig. 4 shows a maneuver aligning the spacecraft to the VNB frame from an initial body orientation congruent to the ECI frame. The simulation is performed for a dawn-dusk SSO orbit with a mean altitude of 250 km, setting $\omega_{RW} = 0$ RPM as initial condition for the four reaction wheels. After about 600 s, $\mathbf{q} \approx [1, 0, 0, 0]$ and both the wind angles are brought to zero with a pointing accuracy in the order of 0.15° rms.

For the same simulation, Fig. 5 shows the evolution of the reaction wheels angular velocity, magnetorquers commanded dipole, and attitude actuators power consumption. The latter is implemented in the form of look-up tables (LUTs) derived from the information available in the actuators datasheet, such as $P_{RW} = LUT(\boldsymbol{\omega}_{RW}, \boldsymbol{\tau}_{RW})$ and $P_{MT} = LUT(\mathbf{m}_{MT})$. The power consumption has a sharp peak in the initial few seconds as the reaction wheels are exerting the maximum torque level. The angular velocity of each reaction wheel remains well below the 6000 RPM saturation limit, gradually reducing its angular momentum thanks to the effect of magnetorquers desaturation.

The tuned attitude controller was always stable for different initial attitude and orbit conditions in the 200 km to 300 km altitude range. However, these results apply to the ideal case of a symmetric platform with uniform mass density, which results in an almost zero residual drag torque in nominal attitude. In reality, platform appendages and CoG deviations with respect to the geometrical center can significantly increase the residual aerodynamic torque as per equation 39. In this regard, we simulated a few cases for different initial altitudes and CoG deviation along the $\mathbf{y}_B$ axis. Coupling with the orbital control is included through the disturbance torque produced by the thruster as per equation 55 and according to the control law defined in equation 57. For a 4.5 hours period propagation, Fig. 6 shows the resulting mean disturbance torque, mean attitude actuators power consumption, and mean rms pointing accuracy.

Clearly, the higher levels of disturbance torques associated to lower altitudes and larger CoG deviation imply an increase in power consumption and some loss in pointing accuracy. Most importantly, as soon as the orbital-averaged value of residual disturbance torque is greater than the control authority of the magnetorquers (in our case, in the order of 1e-5 Nm at maximum dipole level along each axis), the reaction wheels will eventually saturate. Then, the attitude controller fails and the spacecraft dynamics devolves into chaos. To prevent saturation and loss of attitude control, the spacecraft must thus minimize the residual disturbance torques, with a sufficiently high margin allowing to cope with uncertainties in space weather conditions. For example,

This article has been accepted for publication in IEEE Transactions on Aerospace and Electronic Systems. This is the author's version which has not been fully edited and content may change prior to final publication. Citation information: DOI 10.1109/TAES.2025.3577159

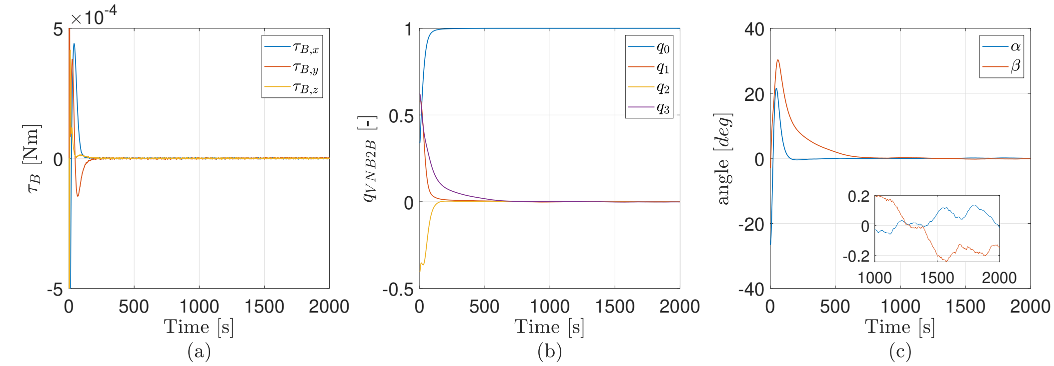

Fig. 4. Evolution of a) body torque, b) attitude quaternion, and c) wind angles during a maneuver aligning the spacecraft to the VNB frame.

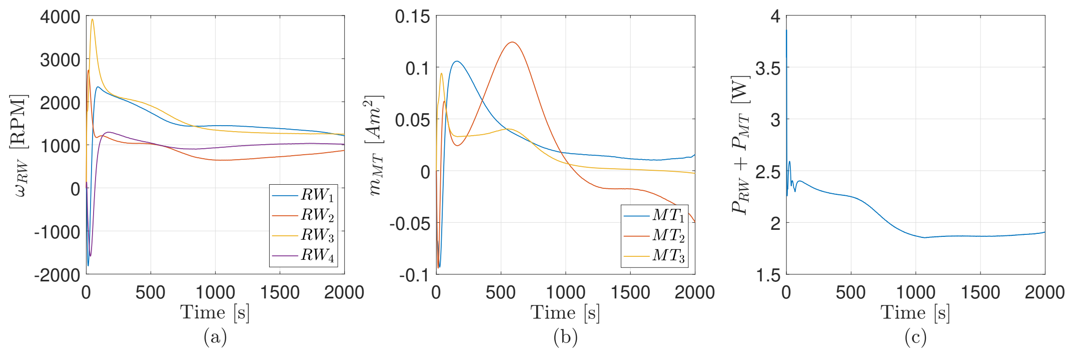

Fig. 5. Evolution of a) reaction wheels angular velocity, b) magnetorquers control dipole, and c) actuators power consumption during a maneuver aligning the spacecraft to the VNB frame.

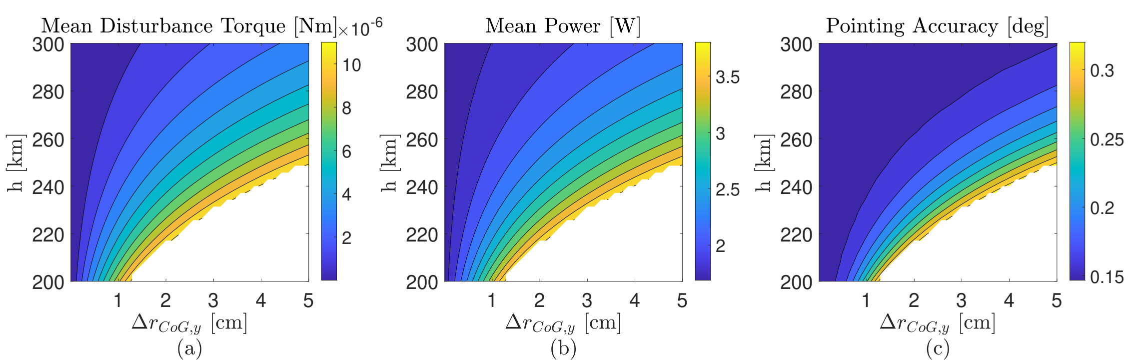

Fig. 6. a) Mean disturbance torque, b) attitude actuators mean power consumption, and c) rms pointing accuracy depending on mean operating altitude and CoG deviation with respect to the platform geometric centre. Blank data points represents attitude control failure.

Fig. 6 illustrates that with a CoG deviation below 1 cm, the spacecraft consistently maintains robust attitude control within the entire 200–300 km altitude range. In this regard, considering nominal operation at 250 km, only very extreme space weather events (typically lasting no more than a few days) would increase atmospheric density to levels similar to those found at, e.g., 200 km, where mean density is approximately five times higher than at 250 km. As such, attitude control safety margin translates into a requirement on the maximum allowable CoG deviation. Additionally, as the ABEP system does not use propellant stored on-board, the spacecraft's CoG position is expected to remain stable over its operational lifetime, further supporting long-term control stability. On the other hand, in case a sufficiently safe stability margin could not be achieved (such as for missions below 200 km of altitude or for highly asymmetric spacecraft mass and geometry configurations), a thruster-based reaction control system or other means, such as passive or active aerosurfaces, must be used to desaturate the on-board angular momentum-exchange devices.

B. Orbit Control and Stability

Maintaining a VLEO orbit for extended periods represents a technical challenge, since the atmospheric drag affects significantly the motion of the spacecraft, leading to a rapid orbit decay. As a reference, Fig. 7 provides the altitude, atmospheric species number density, and longitudinal drag force evolution for a reference unpro-

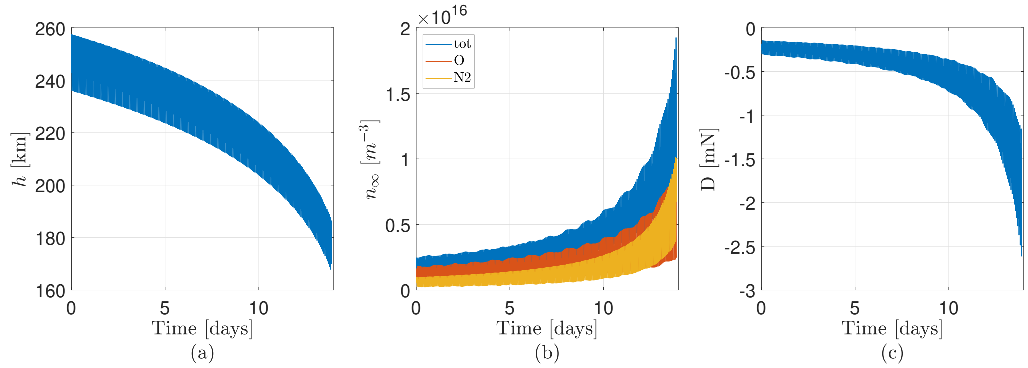

Fig. 7. Evolution of a) mean altitude, b) atmosphere species number density, and c) longitudinal drag for a dawn-dusk SSO with an initial mean altitude of 250 km.

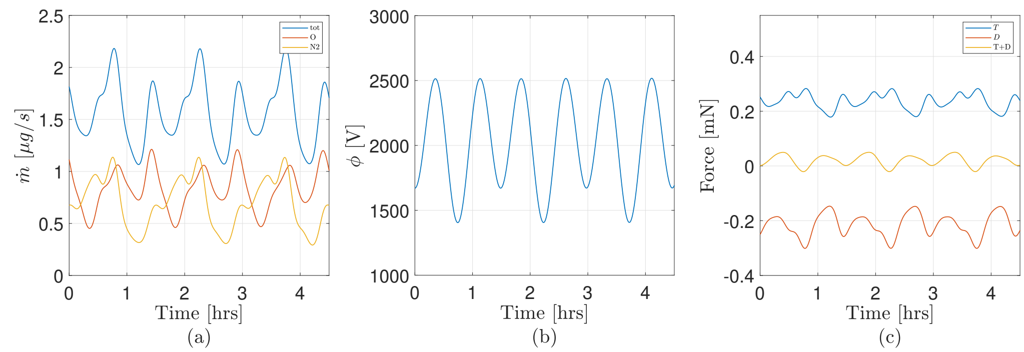

Fig. 8. a) ABEP processed mass flow rate, b) control acceleration voltage, and c) spacecraft longitudinal forces during a three-orbits propagation period.

pelled spacecraft in a dawn dusk SSO orbit. For this and further analyses, we consider a reference orbit with an initial inclination of 96.5 deg, an initial semi-major axis of 6621 km, corresponding to a mean altitude of about 250 km, and an initial eccentricity and true anomaly set to zero. The initial UTC time is set to the 18th of April 2012 at midnight, which for a 6 am orbit results in an initial RAAN of 296.4 deg. The initial time was selected to allow for a 3-year propagation period from 2012 to 2015, capturing solar activity during the peak of Solar Cycle 24 [64]. This period aligns with moderate solar activity, which serves as a representative mean for this analysis. Transients in space weather have been accounted for by linking the NRLMSISE-00 atmospheric model to the F107 81-day average, F107 daily, and Ap magnetic indices observed during the selected propagation period. These parameters have been extracted from the CelesTrack database [65].

As Fig. 7 shows, without thrust compensation, the atmosphere density and drag exponentially increases in time due to the rapid orbit decay. After about two weeks of propagation, the mean altitude is reduced from 250 km down to less than 170 km. From the same initial orbit, we verify the behaviour of the implemented thruster controller. In particular, we set the guidance submodel to target an orbit raising of about 10 km, corresponding to a target mean altitude of about 260 km. We consider an intake collection area of $0.01\ m^2$, a collection efficiency $\eta_c = 0.33$, and a thrust efficiency $\eta_T = 0.33$, evaluating afterwards (through the sensitivity analysis presented in Sec. IIIC) the minimum value they shall have to ensure long-term orbit maintenance and compliance to the platform power budget. The orbit controller proportional gains were manually tuned to the values k_a = 1e-5 $V/m/s$ and k_e = 1e9 Vm/s. The integral term was set to k_i = 1.16e-8 $V/m/s$, meaning that the acceleration voltage is increased or decreased at a rate of 1 V per day per km of semi-major axis deviation with respect to the targeted one. For the case of full dissociation of the processed flow, Fig. 8 shows a detail of the mass flow processed by the thruster, control acceleration voltage, and resulting drag and thrust forces for a three-orbit periods duration. The total atmospheric mass flow and applied voltage respectively oscillates between 1.07 and 2.18 $\mu g/s$ and between 1405 and 2517 V over the propagation period.

While the behaviour highlighted in Fig. 8 implies the need to develop a highly flexible ion thruster, which represents a significant technological challenge, we can appreciate how the implemented control logic seems effective in ensuring a long term orbit maintenance. In particular, Fig. 9 shows the system behaviour during an orbital propagation of three years, comparing the two extreme cases of no flow dissociation and full dissociation

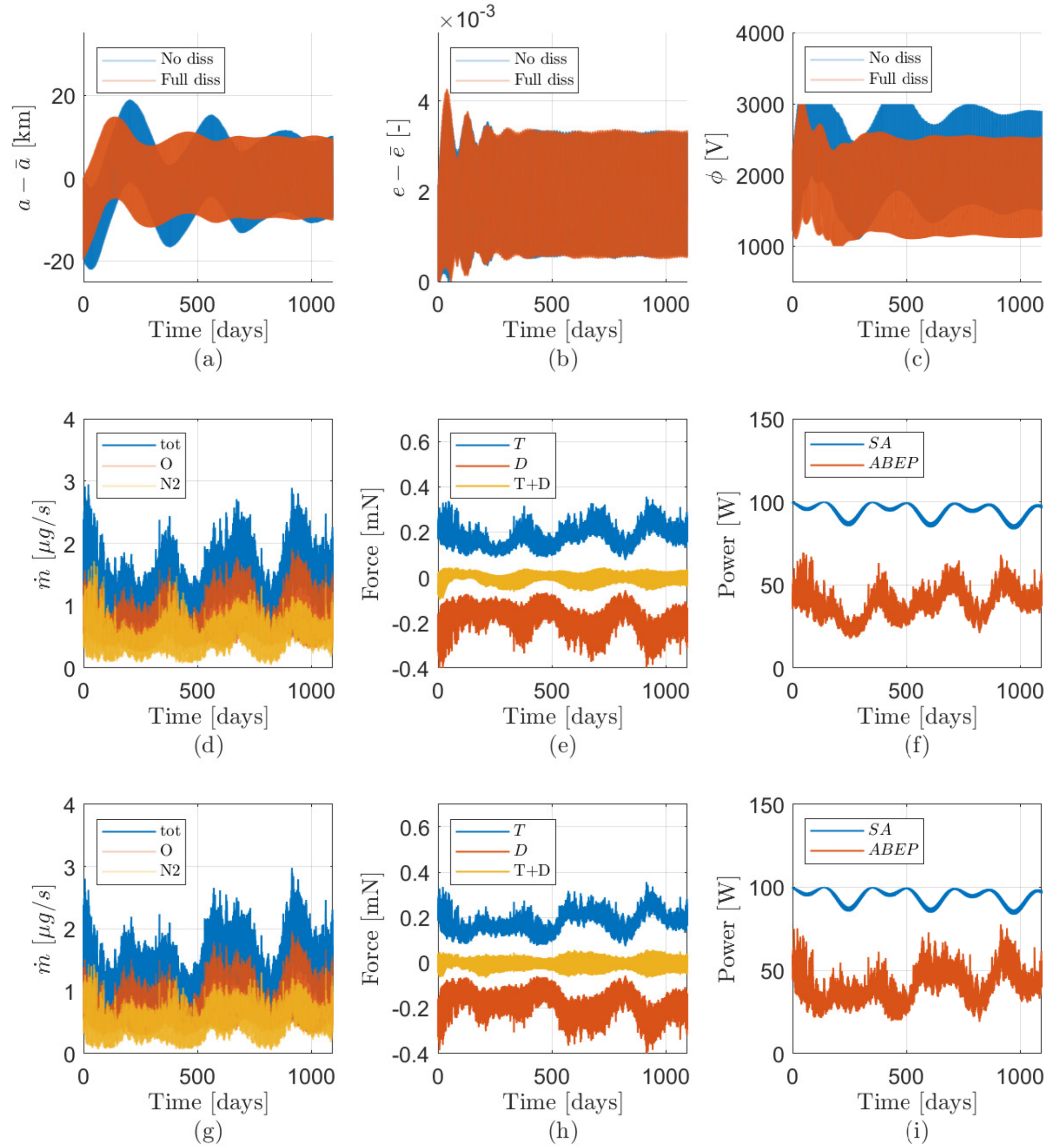

Fig. 9. Evolution during a 3-years orbit propagation period of a) semi-major axis, b) eccentricity error, and c) control voltage for the two extreme cases of full dissociation and null dissociation of the gathered flow. For null dissociation: evolution of d) mass flow rate processes by the thruster, e) drag and thrust forces acting on the platform, and f) ABEP power consumption and power available from the solar arrays. For full dissociation: evolution of g) mass flow rate processes by the thruster, h) drag and thrust forces acting on the platform, and i) ABEP power consumption and power available from the solar arrays.

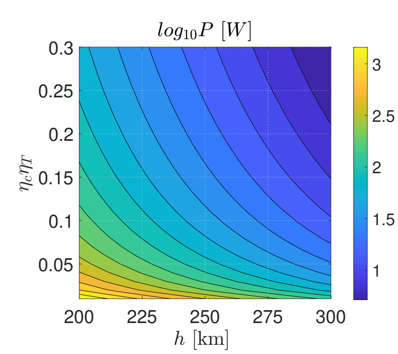

Fig. 10. Mean ABEP power consumption for drag compensation vs altitude and $\eta_c\eta_T$ ranging between 0.01 and 0.3.

in the thruster discharge. Due to the very low resulting net force, the platform slowly performs a 10 km orbit raising throughout a period of about three months. After that, the orbital elements are maintained with high precision. As shown in the detailed view of Fig. 8b, the acceleration voltage significantly oscillates in line with the orbital period to keep the orbit eccentricity low. The mean value of the acceleration voltage is lower for the case of full flow dissociation as the thruster will accelerate a lower molecular mass flow, which for the same acceleration voltage results in higher thrust levels and power consumption compared to the case of null dissociation. Still, we can appreciate how the implemented controller seems robust to the uncertainties in both orbit environment

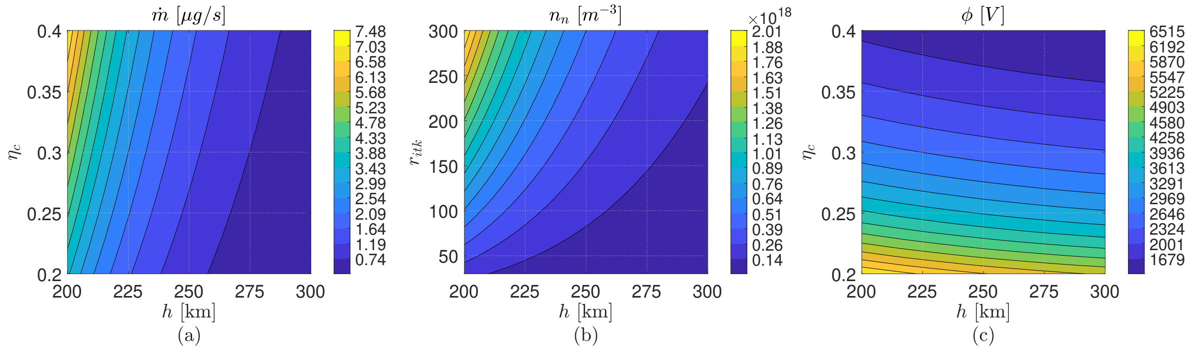

Fig. 11. a) Air-breathing thruster operating mass flow rate vs mean altitude and collection efficiency. b) Maximum achievable neutral density in the thruster control volume vs altitude and intake compression ratio. c) Acceleration voltage needed for drag compensation vs altitude and collection efficiency, in the hypothesis of null flow dissociation.

and thruster discharge characteristics. The average power consumption during the orbit maintenance phase is well below the one available from the solar array.

For what concerns the uncertainties in the thruster discharge behavior, we see that the mean ABEP power consumption is comparable among the null and full dissociation case, with the latter case showing a greater spread in the power profile. Along with the dissociation process, additional sources of uncertainty in determining system performance relate to complex space weather phenomena, which can cause deviations in atmospheric density and composition from the conditions simulated in this work. Typically, space weather uncertainties lead to mean flow density fluctuations of approximately $\pm 50\%$ over timescales of a few weeks or months [64]. Although significant, Fig. 9 demonstrates that the implemented orbit controller effectively manages these large flow property variations, successfully reaching and maintaining the target orbit. However, this comes at the cost of increased propulsion power consumption during periods of higher flow density. In extreme space weather events, such as major solar flares or geomagnetic storms, the satellite could temporarily allocate additional power to the propulsion system to sustain the target orbit. Nonetheless, detailed simulations to optimize power management strategies under such conditions remain an area for future investigation. In this regard, additional mission-specific requirements such as eclipse duration for different target orbits, power available to recharge the battery during sunlight periods, and payload/telecom power consumption and duty cycle must be taken into account to fully explore the capabilities of air-breathing satellites. These factors, including the flexibility of battery operation, will be considered in future work to verify optimal power management during peak demand scenarios.

C. Air-breathing Propulsion Requirements

As apparent from the long-term propagation presented in the previous Section, the ABEP system will eventually provide an average thrust level equal to the drag acting on the whole platform when maintaining a target circular orbit, resulting in a mean net force of zero. Depending on the mean power that the platform could allocate to propulsion, this poses a strict requirement on the minimum collection and thrust efficiencies the propulsion system should guarantee, as well noted in the analysis presented in [18]. For our reference CubeSat platform, and considering orbit-averaged atmosphere properties, Fig. 10 provides an estimation of the mean ABEP power consumption needed for drag compensation vs collection and thrust efficiencies. Fig. 10 shows how, for a given power constraint, the efficiency requirement is significantly relaxed when orbiting at higher altitudes. On the other hand, higher altitude operation implies the need to operate at very low mass flow rates and to ionize a very low density neutral flow, which poses a technological challenge. In particular, the neutral flow density that could be achieved in an air-breathing thruster will depend on the compression level the intake could passively or actively achieve, such as:

$$n_n = r_{itk} \sum_s n_{s,\infty}, \tag{60}$$

where n_n is the neutral density in the thruster control volume, and r_{itk} is the intake compression ratio. Compression values in the 30-300 range have been typically reported in the recent literature [6]. Accordingly, Fig. 11 plots the operating thruster mass flow rate and number density as a function of mean operating altitude, collection efficiency, and intake compression ratio. Fig. 11 also estimates the acceleration voltage needed for compensating the drag, which is affected both by the altitude dependant propellant composition and collection efficiency. For $h = 250$ km and $r_{itk} = 150$, a maximum neutral density $n_n = 2.75e17$ m^{-3} could be achieved, which is indeed about two orders of magnitude lower that the one typical of mature electric propulsion devices such as Hall thrusters or ion engines [17].

Moreover, depending on the required mission lifetime, the higher the altitude the lower will be the actual advantage of using air-breathing propulsion compared to traditional electric propulsion. For our reference platform geometry, about 138 kNs of total impulse would be needed to compensate the drag for a 5 years mission duration at 200 km of altitude, which reduces to 34.1 kNs and 10.7 kNs at a mean altitude of 250 km and 300

This article has been accepted for publication in IEEE Transactions on Aerospace and Electronic Systems. This is the author's version which has not been fully edited and content may change prior to final publication. Citation information: DOI 10.1109/TAES.2025.3577159

km, respectively. This may be compared with the total impulse, in the order of 5.5 kNs, that a highly performing iodine-fed propulsion system can to date provide to a CubeSat.

IV. CONCLUSION

In this study, we presented a preliminary mission analysis of an air-breathing 6U nanosatellite. Using a GNC simulation framework that couples high-fidelity atmospheric and aerodynamic models representative of the VLEO environment with simplified models of the on-board sensors and actuators, the simulations demonstrated the potential of air-breathing electric propulsion to extend the lifespan of low-altitude missions. Through the implementation of a control law regulating the voltage applied to the thruster accelerating electrode, our reference 6U air-breathing CubeSat was able to maintain a target VLEO orbit with high precision for the full three years duration propagation, even under two completely different operating regimes in terms of assumed flow dissociation level in the thruster discharge.

However, our study has some limitations that require further investigation. First, the proposed control logic necessitates the development of highly flexible thrusters capable of operating at very low propellant pressures and across a wide range of acceleration voltages, which may exceed the current technological capabilities. Additionally, the impact of atmospheric variability driven by solar activity, geomagnetic disturbances, and other transient space weather phenomena should be more thoroughly assessed. This includes extending the analysis beyond the selected three-year propagation window by incorporating historical space weather data, as this can significantly influence atmospheric density and composition at VLEO altitudes, with direct consequences on the propulsive performance and orbital stability of the air-breathing platform. In this regard, future research will focus on implementing more advanced plasma and rarefied flow models to better describe the complex physical processes involved in air-breathing discharges. Additionally, efforts will focus on developing optimal power management strategies that account for large uncertainties in space weather, realistic payload and telecommunications power consumption and duty cycle, as well as battery management constraints. In-orbit testing of an air-breathing CubeSat will then be crucial to validate any simulation and refine the design parameters for optimal performance in the highly dynamic VLEO environment.

In conclusion, while this preliminary analysis highlights the significant potential of air-breathing electric propulsion for small-scale VLEO spacecraft, several challenges must be addressed to advance the technology. Particularly, the development of highly-flexible, high-performing thrusters together with the in-orbit experimentation of the concept will be essential steps toward the practical implementation and widespread adoption of air-breathing nanosatellites.

REFERENCES

[1] A. Shao, A. M. Madni, and J. R. Wertz, "Quantifying the effect of orbit altitude on mission cost for earth observation satellites," *54th AIAA Aerospace Sciences Meeting*, 2016.

[2] N. H. Crisp, P. C. Roberts, F. Romano, K. L. Smith, V. T. Oiko, V. Sulliotti-Linner, V. Hanessian, G. H. Herdrich, D. García-Almiñana, D. Kataria, and S. Seminari, "System modelling of very low Earth orbit satellites for Earth observation," *Acta Astronautica*, vol. 187, no. June, pp. 475–491, 2021.

[3] L. Berthoud, R. Hills, A. Bacon, M. Havouzaris-Waller, K. Hayward, J.-D. Gayrard, F. Arnal, and L. Combelles, "Are very low earth orbit (vleo) satellites a solution for tomorrow's telecommunication needs?" *CEAS Space Journal*, Jun. 2022.

[4] C. McGrath, C. Lowe, M. Macdonald, and S. Hancock, "Investigation of very low Earth orbits (VLEOs) for global spaceborne lidar," *CEAS Space Journal*, vol. 14, 2022.

[5] P. Roberts, "1st symposium of very low earth orbit missions and technologies," *CEAS Space Journal*, vol. 14, pp. 605–608, 2022.

[6] T. Andreussi, E. Ferrato, and V. Giannetti, "A review of air-breathing electric propulsion: from mission studies to technology verification," *Journal of Electric Propulsion*, vol. 1, no. 1, pp. 1–57, 2022.

[7] P. Zheng, J. Wu, Y. Zhang, and B. Wu, "A comprehensive review of atmosphere-breathing electric propulsion systems," *International Journal of Aerospace Engineering*, vol. 2020, no. 4, 2020.

[8] A. Filatyev, A. Golikov, A. Erofeev, S. Khartov, A. Lovtsov, D. Padalitsa, V. Skvortsov, and O. Yanova, "Research and development of aerospace vehicles with air breathing electric propulsion: Yesterday, today, and tomorrow," *Progress in Aerospace Sciences*, vol. 136, p. 100877, 2023.

[9] M. Tagawa, K. Yokota, K. Nishiyama, H. Kuninaka, Y. Yoshizawa, D. Yamamoto, and T. Tsuboi, "Experimental study of air breathing ion engine using laser detonation beam source," *Journal of Propulsion and Power*, vol. 29, no. 3, pp. 501–506, 2013.

[10] T. Andreussi, G. Cifali, V. Giannetti, A. Piragino, E. Ferrato, A. Rossodivita, M. Andrenucci, J. Longo, and L. Walpot, "Development and Experimental Validation of a Hall Effect Thruster RAM-EP Concept," *35th International Electric Propulsion Conference, Atlanta, Georgia, IEPC-2017-377*, 2017.

[11] V. Hruby, K. Hohman, and J. Szabo, "Air Breathing Hall Effect Thruster Design Studies and Experiments," *37th International Electric Propulsion Conference, Boston, Massachusetts, IEPC-2022-446*, 2022.

[12] F. Romano, B. Massuti-Ballester, T. Binder, G. Herdrich, S. Fasoulas, and T. Schönherr, "System analysis and test-bed for an atmosphere-breathing electric propulsion system using an inductive plasma thruster," *Acta Astronautica*, vol. 147, no. March 2017, pp. 114–126, 2018.

[13] T. Andreussi, E. Ferrato, C. A. Paissoni, A. Kitaeva, V. Giannetti, A. Piragino, S. Schäff, K. Katsonis, C. Berenguer, Z. Kovacova, E. Neubauer, M. Tisaev, B. Karadag, A. Lucca Fabris, M. Smirnova, A. Mingo, D. Le Quang, Z. Alsalihi, F. Bariselli, P. Parodi, P. Jorge, and T. E. Magin, "The AETHER project: development of air-breathing electric propulsion for VLEO missions," *CEAS Space Journal*, Apr. 2022.

[14] M. Y. Ovchinnikov, Y. V. Mashtakov, and D. S. Roldugin, "Mathematical Modeling of the Dynamics of a Low-Flying Spacecraft with a Ramjet Electric Propulsion Engine," *Mathematical Models and Computer Simulations*, vol. 14, p. 452–465, 2022.

[15] S. Vaidya, C. Traub, F. Romano, S. Rodriguez-Donaire, D. Garcia-Almiñana, M. Sureda, and M. Garcia-Berenguer, "Development and analysis of novel mission scenarios based on atmosphere-breathing electric propulsion (abep)," *CEAS space journal*, pp. 1–18, 03 2022.

[16] P. Crandall and R. Wirz, "Air-breathing electric propulsion: mission characterization and design analysis," *Journal of Electric Propulsion*, vol. 1, no. 12, pp. 931–937, 2022.

[17] M. Tisaev, E. Ferrato, V. Giannetti, C. Paissoni, N. Baresi, A. Lucca Fabris, and T. Andreussi, "Air-breathing electric propul-

sion: Flight envelope identification and development of control for long-term orbital stability," *Acta Astronautica*, vol. 191, no. October 2021, pp. 374–393, 2022.

[18] V. Giannetti, E. Ferrato, and T. Andreussi, "On the critical parameters for feasibility and advantage of air-breathing electric propulsion systems," *Acta Astronautica*, vol. 220, pp. 345–355, 2024.

[19] *ERC GA 101088694: BREATHE- Building a space Revolution: Electric Air-breathing Technology for High-atmosphere Exploration*.

[20] Woodley, A., Horstman, E., Keidar, M., and al. , "Requirements for air-breathing electric propulsion in low-altitude," *J Electr Propuls*, vol. 3, p. 34, 2024.

[21] S. Andrews, R. Andriulli, N. Souhair, M. Magarotto, and F. Ponti, "Cathode-less rf plasma thruster design and optimisation for an atmosphere-breathing electric propulsion (abep) system," *Acta Astronautica*, vol. 225, pp. 833–844, 2024.

[22] G. Herdrich, K. Papavramidis, P. Maier, J. Skalden, F. Hild, J. Beyer, M. Pfeiffer, M. Fugmann, S. Klinker, S. Fasoulas, N. Souhair, F. Ponti, M. Walther, A. Wiegand, L. Walpot, B. Duesmann, E. Borras, P. Roberts, and N. Crisp, "System design study of a vleo satellite platform using the irs rf helicon-based plasma thruster," *Acta Astronautica*, vol. 215, pp. 245–259, 2024.

[23] J. Lopez-Uricoechea, D. Lev, and M. L. R. Walker, "0-d composition and performance analysis of an air-breathing radiofrequency ion thruster," *Journal of Electric Propulsion*, vol. 1, no. 1, 2022.

[24] X. Zuo, M. Xu, M. Huang, M. Li, and N. Peng, "Maintenance strategy for elliptical orbit satellite with air-breathing electric propulsion," *IEEE Transactions on Aerospace and Electronic Systems*, vol. 59, no. 5, pp. 6863–6877, 2023.

[25] F. A.S. and Y. O.V., "The optimal control by the thrust vector of air-breathing electric propulsion to maximize the apogee altitude of orbit with an ultra-low perigee," *Kosmičeskie issledovaniâ*, vol. 61, pp. 163–176, 2023.

[26] A. Golikov and A. Filatyev, "Integrated optimization of trajectories and layout parameters of spacecraft with air-breathing electric propulsion," *Acta Astronautica*, vol. 193, pp. 644–652, 2022.

[27] Y. Yue, J. Geng, G. Feng, and W. Li, "Elliptical orbit design based on air-breathing electric propulsion technology in very-low earth orbit space," *Aerospace*, vol. 10, 10 2023.

[28] *Terran Orbital website*, accessed: 2024-07-10.

[29] N. K. Pavlis, S. A. Holmes, S. C. Kenyon, and J. K. Factor, "The development and evaluation of the earth gravitational model 2008 (egm2008)," *Journal of Geophysical Research: Solid Earth*, vol. 117, no. B4, 2012.

[30] D. A. Vallado, *Fundamental of Astrodynamics and Applications*. Microcosm, El Segundo, CA, 2001.

[31] J. L. J. ByJohn L. Crassidis, *Optimal Estimation of Dynamic Systems*. Chapman and Hall/CRC, 2004.

[32] M. E. Pittelkau, "Rotation vector in attitude estimation," *Journal of Guidance, Control, and Dynamics*, vol. 26, no. 6, pp. 855–860, 2003.

[33] J. Picone, A. E. Hedin, D. P. Drob, and A. C. Aikin, "NRLMSISE-00 empirical model of the atmosphere:Statistical comparisons and scientific issues," *Journal of Geophysical Research*, vol. 107, no. A12, p. 1468, 2002.

[34] L. A. Sinpetru, N. H. Crisp, D. Mostaza-Prieto, S. Livadiotti, and P. C. Roberts, "Adbsat: Methodology of a novel panel method tool for aerodynamic analysis of satellites," *Computer Physics Communications*, vol. 275, 2022.

[35] L. A. Sinpetru, N. H. Crisp, P. C. Roberts, V. Sulliotti-Linner, V. Hanessian, G. H. Herdrich, F. Romano, D. Garcia-Almiñana, S. Rodríguez-Donaire, and S. Seminari, "Adbsat: Verification and validation of a novel panel method for quick aerodynamic analysis of satellites," *Computer Physics Communications*, vol. 275, p. 108327, 2022.

[36] P. A. Chambre and S. A. Schaaf, "Flow of rarefied gases," *Princeton University Press*, 1961.

[37] D. P. Drob, J. T. Emmert, J. W. Meriwether, J. J. Makela, E. Doornbos, M. Conde, G. Hernandez, J. Noto, K. A. Zawdie, S. E. McDonald, J. D. Huba, and J. H. Klenzing, "An update to the horizontal wind model (hwm): The quiet time thermosphere," *Earth and Space Science*, vol. 2, no. 7, pp. 301–319, 2015.

[38] B. Wie, H. Weiss, and A. Arapostathis, "Quarternion feedback regulator for spacecraft eigenaxis rotations," *Journal of Guidance, Control, and Dynamics*, vol. 12, no. 3, pp. 375–380, 1989.

[39] F. Romano, J. Espinosa-Orozco, M. Pfeiffer, G. Herdrich, N. H. Crisp, P. C. Roberts, B. E. Holmes, S. Edmondson, S. Haigh, S. Livadiotti, A. Macario-Rojas, V. T. Oiko, L. A. Sinpetru, K. Smith, J. Becedas, V. Sulliotti-Linner, M. Bisgaard, S. Christensen, V. Hanessian, T. K. Jensen, J. Nielsen, Y. A. Chan, S. Fasoulas, C. Traub, D. García-Almiñana, S. Rodríguez-Donaire, M. Sureda, D. Kataria, B. Belkouchi, A. Conte, S. Seminari, and R. Villain, "Intake design for an Atmosphere-Breathing Electric Propulsion System (ABEP)," *Acta Astronautica*, vol. 187, no. May, pp. 225–235, 2021.

[40] P. Zheng, J. Wu, Y. Zhang, and Y. Zhao, "Design and Optimization of vacuum Intake for Atmosphere-Breathing electric propulsion (ABEP) system," *Vacuum*, vol. 195, jan 2022.

[41] E. Ferrato, V. Giannetti, M. Tisaev, A. Lucca Fabris, F. Califano, and T. Andreussi, "Rarefied Flow Simulation of Conical Intake and Plasma Thruster for Very Low Earth Orbit Spaceflight," *Frontiers in Physics*, vol. 10, no. March, pp. 1–17, 2022.

[42] C. Rapisarda, P. C. E. Roberts, and K. L. Smith, "Design and optimisation of a passive atmosphere-breathing electric propulsion (abep) intake," *Acta Astronautica*, 2022.

[43] G. Moon, M. Yi, K. Park, Y. Kim, H. Yoon, and E. Jun, "Performance characterization and kinetic analysis of atmosphere-breathing electric propulsion intake device," *Vacuum*, vol. 212, p. 112066, 2023.

[44] K. Mrózek, T. Dytrych, P. Moliš, V. Dániel, and A. Obrusník, "Global plasma modeling of a magnetized high-frequency plasma source in low-pressure nitrogen and oxygen for air-breathing electric propulsion applications," *Plasma Sources Science and Technology*, vol. 30, no. 12, 2021.

[45] E. Ferrato, V. Giannetti, F. Califano, and T. Andreussi, "Atmospheric propellant fed hall thruster discharges: 0d-hybrid model and experimental results," *Plasma Sources Science and Technology*, vol. 31, no. 7, p. 075003, jul 2022.

[46] F. Taccogna, F. Cichocki, and P. Minelli, "Coupling plasma physics and chemistry in the PIC model of electric propulsion: Application to an air-breathing, low-power Hall thruster." *Front. Phys.*, vol. 10, 2022.

[47] P. Zheng, J. Wu, Y. Zhang, B. Che, and Y. Zhao, "An atmosphere-breathing propulsion system using inductively coupled plasma source," *Chinese Journal of Aeronautics*, vol. 36, no. 5, pp. 223–238, 2023.

[48] G. Moon, W. Choe, and E. Jun, "Plasma plume simulation of an atomic oxygen-fed ion thruster in very-low-earth-orbit," *Plasma Sources Science and Technology*, vol. 32, no. 12, dec 2023.

[49] S. Mazouffre, "Electric propulsion for satellites and spacecraft: established technologies and novel approaches." *Plasma Sources Science and Technology*, 2016.

[50] V. Giannetti, A. Piragino, C. A. Paissoni, E. Ferrato, D. Estublier, and T. Andreussi, "Experimental scaling laws for the discharge oscillations and performance of hall thrusters," *Journal of Applied Physics*, vol. 131, 1 2022.

[51] H. Schaub, S. R. Vadali, J. L. Junkins, and K. T. Alfriend, "Spacecraft formation flying control using mean orbit elements," *Journal of the Astronautical Sciences*, vol. 48, no. 1, 2000.

[52] P. Gurfil, "Control-theoretic analysis of low-thrust orbital transfer using orbital elements," *Journal of Guidance, Control, and Dynamics*, vol. 26, no. 6, 2003.

[53] L. Breger and J. P. How, "Gauss's variational equation-based dynamics and control for formation flying spacecraft," *Journal of Guidance, Control, and Dynamics*, vol. 30, no. 2, pp. 437–448, 2007.

[54] A. Garulli, A. Giannitrapani, M. Leomanni, and F. Scortecci, “Autonomous low-earth-orbit station-keeping with electric propulsion,” *Journal of Guidance, Control, and Dynamics*, vol. 34, no. 6, pp. 1683–1693, 2011.

[55] P. Alken, E. Thébault, C. Beggan, H. Amit, J. Aubert, J. Baerenzung, T. Bondar, W. Brown, S. Califf, A. Chambodut, A. Chulliat, G. Cox, C. Finlay, A. Fournier, N. Gillet, A. Grayver, M. Hammer, M. Holschneider, L. Huder, G. Hulot, T. Jager, C. Kloss, M. Korte, W. Kuang, A. Kuvshinov, B. Langlais, J.-M. Léger, V. Lesur, P. Livermore, F. Lowes, S. Macmillan, W. Magnes, M. Mandea, S. Marsal, J. Matzka, M. Metman, T. Minami, A. Morschhauser, J. Mound, M. Nair, S. Nakano, N. Olsen, F. Pavón-Carrasco, V. Petrov, G. Ropp, M. Rother, T. Sabaka, S. Sanchez, D. Saturnino, N. Schnepf, X. Shen, C. Stolle, A. Tangborn, L. Tøffner-Clausen, H. Toh, J. Torta, J. Varner, F. Vervelidou, P. Vigneron, I. Wardinski, J. Wicht, A. Woods, Y. Yang, Z. Zeren, and B. Zhou, “International Geomagnetic Reference Field: the thirteenth generation,” *Earth, Planets and Space*, vol. 73, 2021.

[56] W. M. Folkner, J. G. Williams, and D. H. Boggs, “The Planetary and Lunar Ephemeris DE 421,” *IPN Progress Report 42–178*, 2009.

[57] NanoTorque GSW600 Reaction Wheel datasheet, Accessed: 2025-04-08, https://gomspace.com/UserFiles/Subsystems/datasheet/gs-ds-nanotorque-gsw-600-23.pdf.

[58] NanoTorque GST600 Magnetorquer datasheet, Accessed: 2025-04-08, https://gomspace.com/UserFiles/Subsystems/datasheet/gs-ds-nanotorque-gst-600-13.pdf.

[59] NanoSense Fine Sun Sensor datasheet, Accessed: 2025-04-08, https://gomspace.com/UserFiles/Subsystems/datasheet/gs-ds-nanosense-fss-31.pdf.

[60] Twinkle Star Tracker datasheet, Accessed: 2025-04-08, https://www.arcsec.space/twinkle/.

[61] NanoSense M315 Magnetometer datasheet, Accessed: 2025-04-08, https://gomspace.com/UserFiles/Subsystems/datasheet/gs-ds-nanosense-m315-12.pdf.

[62] InvenSense MPU-3300 Gyro datasheet, Accessed: 2025-04-08, https://invensense.tdk.com/wp-content/uploads/2015/02/MPU-3300-Datasheet1.pdf.

[63] Novatel OEM719 GPS Receiver datasheet, Accessed: 2025-04-08, https://novatel.com/products/receivers/gnss-gps-receiver-boards/oem719.

[64] Jackson, David R., Bruinsma, Sean, Negrin, Sandra, Stolle, Claudia, Budd, Chris J., Dominguez Gonzalez, Raul, Down, Emily, Griffin, Daniel J., Griffith, Matthew J., Kervalishvili, Guram, Lubián Arenillas, Daniel, Manners, James, Matzka, Jürgen, Shprits, Yuri Y., Vasile, Ruggero, and Zhelavskaya, Irina S., “The space weather atmosphere models and indices (swami) project: Overview and first results,” *J. Space Weather Space Clim.*, vol. 10, p. 18, 2020.

[65] CelesTrack website, https://celestrak.org/spacedata/, Accessed: 2024-04-08.

Eugenio Ferrato received the M.S. degree in Space Engineering in 2017 from the University of Pisa, Pisa, Italy, and the Ph.D. degree in Physics in 2023 from the University of Pisa, Pisa, Italy. He is currently a Research Fellow at the Institute of Mechanical Intelligence at Scuola Superiore Sant’Anna, Pisa, Italy.

He was an Electric Propulsion System Engineer at SITAEL, and he is now the co-founder and Executive Director of Celeste S.r.l., a spin-off company of the Scuola Superiore Sant’Anna. His main research interests are plasma physics and advanced space systems.

Dr. Ferrato is a member of the Electric Rocket Propulsion Society (ERPS).

Vittorio Giannetti received the M.S. degree in space engineering in 2015 from the University of Pisa, Pisa, Italy, and the Ph.D. degree in Aerospace Engineering in 2022 from the University of Pisa, Pisa, Italy. He is currently an Assistant Professor at the Institute of Mechanical Intelligence at Scuola Superiore Sant’Anna, Pisa, Italy.

He was a Propulsion System Engineer at Airbus Defence & Space and a Senior Electric Propulsion Engineer at SITAEL. He is now the co-founder and Chief Executive Officer of Celeste S.r.l., a spin-off company of the Scuola Superiore Sant’Anna. His main research interests are advanced space propulsion systems, plasma physics, and plasma technologies.

Dr. Giannetti is a member of the Electric Rocket Propulsion Society (ERPS) and he is the recipient of the 2024 Kuriki Award for Young Professionals in the field of Electric Propulsion.

Tommaso Andreussi received the M.S. degree in space engineering in 2003 from the University of Pisa and the Scuola Superiore di Studi Universitari e di Perfezionamento Sant’Anna, Pisa, Italy, and the Ph.D. degree in mathematics for the technology and the industry in 2008 from the Scuola Normale Superiore, Pisa, Italy. He is currently a Full Professor at the Institute of Mechanical Intelligence at Scuola Superiore Sant’Anna, Pisa, Italy.

He was the Technical Manager of the Electric Propulsion Research and Development team at SITAEL, and he is a co-founder of Celeste S.r.l., a spin-off company of the Scuola Superiore Sant’Anna. His main research interests are fluid dynamics, plasma physics, and space propulsion.

Prof. Andreussi is a member of the Electric Rocket Propulsion Society (ERPS), the Italian Physical Society (SIF), the Italian Aeronautic and Astronautic Association (AIDAA), and the National Inter-University Consortium for Telecommunications (CNIT).